Batteries & Supercaps

Research Article
doi.org/10.1002/batt.202400466

Chemistry
Europe
European Chemical
Societies Publishing

www.batteries-supercaps.org

# 3D Ternary Hybrid of VSe$_2$/e-MXene/CNT with a Promising Energy Storage Performance for High Performance Asymmetric Supercapacitor

Pavithra Siddu,[a] Sree Raj K A,[b] Sithara Radhakrishnan,[a] Sang Mun Jeong,*[b] and Chandra Sekhar Rout*[a, b]

MXene and TMDs are two of the emerging electrode materials for supercapacitors owing to their unique physicochemical properties such as high conductivity, large surface area, and rich redox active sites. However, sheet restacking, volume expansion and oxidation hinder these materials from being used in practical applications. In this work, a 3D ternary hybrid structure of metallic VSe$_2$, Ti$_3$C$_2$T$_x$ MXene and carbon nanotube was designed to address some of the challenges in 2D materials-based electrodes for supercapacitor application. The exfoliated MXene and CNT decorated VSe$_2$ 3D structure showed excellent synergy between each component to deliver promising energy storage and cycling performance. The ternary hybrid structure also can suppress the surface oxidation of MXene sheets during the hydrothermal reaction. Furthermore, an asymmetric supercapacitor fabricated with VSe$_2$/e-MXene/CNT and MoS$_2$/MXene delivered the highest energy density of 35.91 Wh/kg at a power density of 1280 W/kg and a remarkable cycle life.

## 1. Introduction

What makes supercapacitors distinct from batteries is their high-power density, long cycle operation, and charge-discharge mechanism at higher current densities.[1,2] However, these devices have yet to reach their true potential due to low energy storage capability compared to batteries. The research to develop high-performing electrode materials for supercapacitors is going at a brisk pace. Supercapacitor electrodes are predominantly classified into electric double-layer capacitors (EDLCs) and pseudocapacitors based on their charge storage mechanisms.[3] Researchers are trying to enhance the energy density of supercapacitors to a competing range while keeping their high power density and excellent cyclic stability .[4,5] Even though traditional carbon-based materials like graphene,[6] carbon nanotubes,[7] and activated carbon[8] are dominated as supercapacitor electrodes, scientific community is seeking effective alternatives. Recent developments in two-dimensional (2D) nanomaterials as electrodes indicate an optimistic future for supercapacitors. The large active sites and open ion transport channels of 2D materials contribute to their energy storage capabilities.[9,10]

MXenes are a class of 2D materials, with a chemical composition commonly represented as M$_{n+1}$X$_n$T$_x$, where M denotes a transition metal, X represents nitrogen or carbon and T$_x$ stands for surface functional groups (−OH, -F, and -O). MXenes are usually synthesised by selective etching of A layer in the bulk MAX phase in which A signifies an element from the IIA or IIIA group. MAX phases can also be referred to as A layer-bonded layered 2D transition metal nitride and carbide phases.[11–13] Ti$_3$C$_2$, a well-known MXene, is made by selectively etching the aluminium layer from its Ti$_3$AlC$_2$ MAX phase. Ti$_3$C$_2$ MXene exhibits superior pseudocapacitive functionality in practically every electrolyte medium.[14,15] However, the energy-storage capability of individual MXene electrodes is limited by some challenges, such as agglomeration, stability, and the tendency of the multilayer structure to undergo spontaneous collapse during initial cycles. There are multiple material engineering techniques have explored to overcome these issues. One such method is the formation of hybrid structures with MXenes using other nanostructures. 1D and 2D materials like CNT and transition metal dichalcogenides (TMDs) can be combined synergistically with MXene to enhance their supercapacitor performance further.[16–20]

Among the 2D TMDs, vanadium diselenide (VSe$_2$) is an interesting candidate which has demonstrated remarkable energy storage capability as the supercapacitor electrode due to its metallic behaviour in stable state, high surface area and large van der Waals gaps.[21,22] Recently there have been multiple reports of VSe$_2$ and its hybrids with carbon matrices and MXene for supercapacitors[23,24] 1T-VSe$_2$/MXene,[25] VSe$_2$/CNT,[26] VSe$_2$/SWCNTs/rGO[27] are rGO/ VSe$_2$[28] are some of the reported materials with significant energy storage capabilities. These hybrid structures reduce the drawbacks of the individual

[a] P. Siddu, S. Radhakrishnan, C. Sekhar Rout
Centre for Nano and Material Sciences, Jain (Deemed-to-be University), Jain Global Campus, Kanakapura Road, Karnataka, Bangalore 562112, India
E-mail: csrout@gmail.com
        r.chandrasekhar@jainuniversity.ac.in

[b] S. R. K A, S. Mun Jeong, C. Sekhar Rout
Department of Chemical Engineering, Chungbuk National University, Cheongju, Chungbuk 28644, Republic of Korea
E-mail: smjeong@chungbuk.ac.kr

nanostructures and improve the energy storage performance and cycle life of the electrode.

In this work, a ternary hybrid structure of VSe$_2$/e-MXene/CNT was constructed in a typical one-step hydrothermal method. This ternary hybrid showed not only superior energy storage capability but also provided structural stability to the electrode by reducing the oxidation of the MXene surface during the hydrothermal procedure. The ternary hybrid prevents the agglomeration and restacking of both the 2D materials. Subsequently, an asymmetric supercapacitor (ASC) has been assembled with VSe$_2$/e-MXene/CNT as positive and MoS$_2$/MXene negative electrodes, respectively. The assembled ASC exhibits the highest energy density of 35.91 Wh/kg at a power density of 1280 W/kg with a ~99% capacitance retention after 5000 charge$-$discharge cycles.

## Experimental

### Materials

Ammonium metavanadate (NH$_4$VO$_3$), ammonium molybdate tetrahydrate ((NH$_4$)$_6$Mo$_7$O$_{24}$·4H$_2$O), thiourea (CH$_4$N$_2$S), and formic acid were purchased from SDFCL (AR grade), Selenium dioxide (SeO$_2$ 99% LR) was obtained from Himedia, Single-walled carbon nanotube (SWCNT) (Reinste made, prepared by plasma torch synthesis), titanium aluminium carbide (Ti$_3$AlC$_2$) purchased from Y-Carbon Ltd.; Ukraine, Sulfuric acid (H$_2$SO$_4$, 98%, Merck), nitric acid (HNO$_3$, 69–72%, Merck), Lithium Fluoride (LiF, 40% SDFCL), and deionized (DI) water.

### Etching of Ti$_2$AlC$_2$

First, 1.2 g LiF was dissolved in 20 ml of 9 M HCL under constant stirring. 1 g Ti$_2$AlC$_2$ MAX phase was then slowly added to the LiF/ HCl etching solution. The mixture was continuously stirred for 48 h at room temperature in a closed Teflon container. After the etching process residues were collected and washed with DI water and ethanol until the mixture solution became neutral. The MXene produced is collected by vacuum drying for 12 h. Exfoliated MXene (e-MXene) was prepared by ultrasonicating the etched MXene in a centrifuge tube under the Ar atmosphere for 4 h followed by freeze drying for 2 days.

### Synthesis of VSe$_2$/e-MXene/CNT Ternary Hybrid

118 mg of NH$_4$VO$_3$ and 278 mg SeO$_2$ were dissolved completely in a solution containing 25 ml of DI water and 5 ml of formic acid. The freshly prepared 20 mg e-MXene and functionalised SWCNT (30 and 50 mg, from now onwards we will mention it simply as CNT) were added into the above solution and kept under sonication for 5 minutes to attain uniform dispersion. Then the dispersion was transferred into a Teflon-lined stainless-steel autoclave with a capacity of 50 ml. The sealed autoclave was kept at a room temperature of 200 °C for 24 h. After the completion of the hydrothermal reaction, the product is washed and dried in a vacuum oven for 12 h. Figure 1 displays the schematic illustration of the synthesis procedure. Similarly, VSe$_2$/e-MXene and pristine VSe$_2$ were synthesised in the exact experimental conditions without the addition of CNT and e-MXene respectively.

## 2. Material Characterization

The crystal structure of the synthesised sample was analysed using X-ray diffraction (XRD) (Rigaku Ultima IV X-ray diffractometer having Ni-filter for Cu Kα radiation (wavelength, $\lambda =$ 0.1541 nm)). The morphological study of the samples was carried out using a field emission scanning electron microscope (FESEM, JEOL JSM-7100F, JEOL Ltd., Singapore, with a maximum operating accelerating voltage of 30 kV), High-resolution trans-
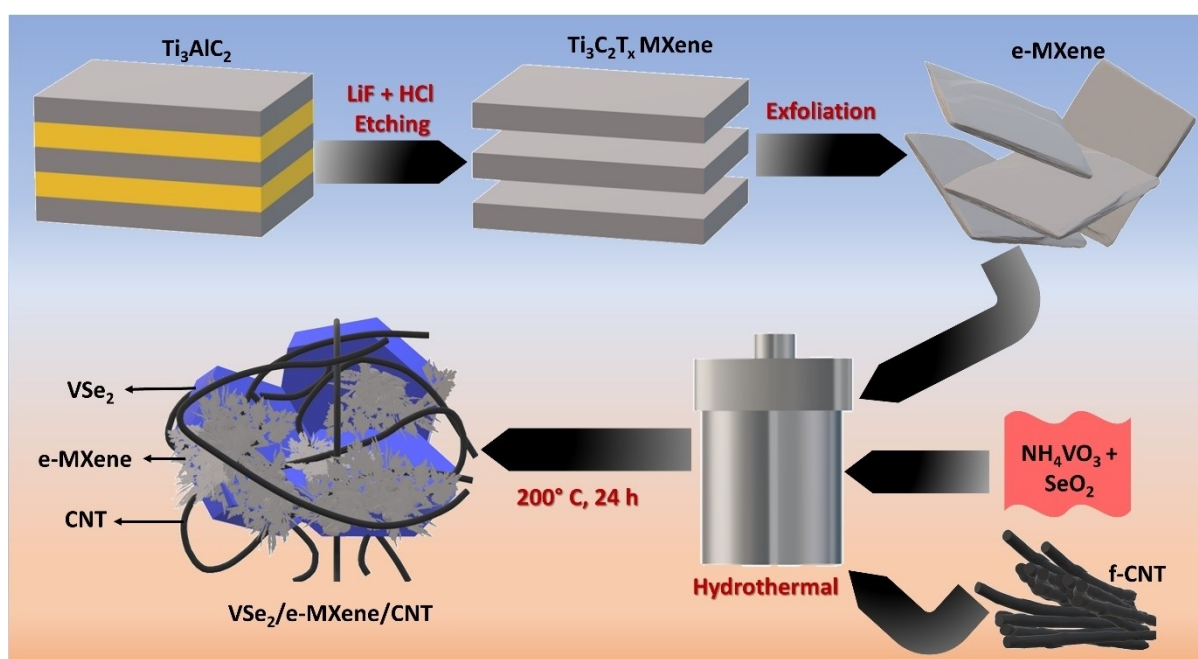


**Figure 1.** Schematic illustration of the MXene etching and VSe$_2$/e-MXene/CNT synthesis.

mission electron microscopy (HRTEM, JEM-2100F, UHR, JEOL) was carried out to study the microstructural details of the samples. X-ray photoelectron spectroscopy (XPS, PHI Quantera II) was used to study the chemical compositions on the material surface.

## 2.1. Electrochemical Characterization

Electrochemical analyses were carried out using the Wuhan Corrtest electrochemical workstation version 5.3. For three-electrode measurements, a working electrode was prepared by drop casting 1.2 mg of active material mixed with isopropyl alcohol and a Nafion binder on a nickel foam substrate. After coating the electrodes were dried in a vacuum oven and pressed using a hydraulic press before use. The three-electrode cell was assembled using an Ag/AgCl reference electrode, Pt counter and 0.5 $K_2SO_4$ aqueous electrolyte. The cyclic voltammetry (CV) and galvanostatic charge-discharge (GCD) tests were in a working potential window of $-0.2$–$0.6$ V. The asymmetric supercapacitor (ASC) was constructed in a typical Swagelok cell with 0.5 $K_2SO_4$ aqueous electrolyte and Whatman filter paper as a separator. Working electrodes were prepared in a similar manner which then cut into a circular shape.

## 3. Results and Discussion

### 3.1. Structural and Morphological Characterization

Figure 1 depicts MXene etching, its exfoliation and the formation of $VSe_2$/e-MXene/CNT ternary hybrid structure. FESEM images of the synthesised materials are provided in Figure 2. Pristine $VSe_2$ shows the morphology of large hexagonal sheets

(Figure 2a and b) which is in tandem with previous studies.[29,30] In $VSe_2$/e-MXene, exfoliated MXene sheets are being decorated on the surface of $VSe_2$ (Figure 2c and d). The exfoliated MXene sheets form a flocs-like structure meanwhile the appearance of $VSe_2$ is changed into a cuboid-like shape. The presence of small MXene sheets with functional groups has an impact on the growth of directions of $VSe_2$ which causes a morphological shift into a cuboid. Previous reports suggest $VSe_2$ can be a "shape-shifter" in the presence of other materials .[31,32] While in $VSe_2$/e-MXene/CNT ternary structure, $VSe_2$ regains its hexagonal appearance with MXene flocs decorations and SWCNT crosslinks (Figure 2e and f). In our previous studies, we observed that in the presence of CNT, $VSe_2$ did not undergo a morphological transition.[33] Because of this, we believe that the morphological change of $VSe_2$ caused by small MXene sheets in the binary structure has been nullified by the presence of CNT in the ternary structure. More studies are required to understand the drastic morphological changes in $VSe_2$ crystals in the presence of other nanomaterials and modifications. There is also a possibility of employing MXenes for the morphological engineering of other 2D materials. Both of these possibilities can open doors to exciting realms in material engineering but are out of the scope of this study. The EDS elemental mapping of the $VSe_2$/e-MXene/CNT shows the uniform distribution of V, Se, Ti, and C in the sample (**Figure S1**).

The XRD pattern of e-MXene is provided in **Figure S2**. After exfoliation, the interlayer distance of MXene is widened to ~1.33 nm. **Figure 3** shows the XRD patterns of $VSe_2$, $VSe_2$/e-MXene and $VSe_2$/e-MXene/CNT. The XRD patterns of all the hybrids are similar to that of pristine $VSe_2$, which completely matches with JCPDS card number 89–1641 confirming the successful formation of $VSe_2$. We did not observe any diffraction patterns of either MXene or CNT in both hybrids due to the high crystalline nature of $VSe_2$ as well as their low concen-
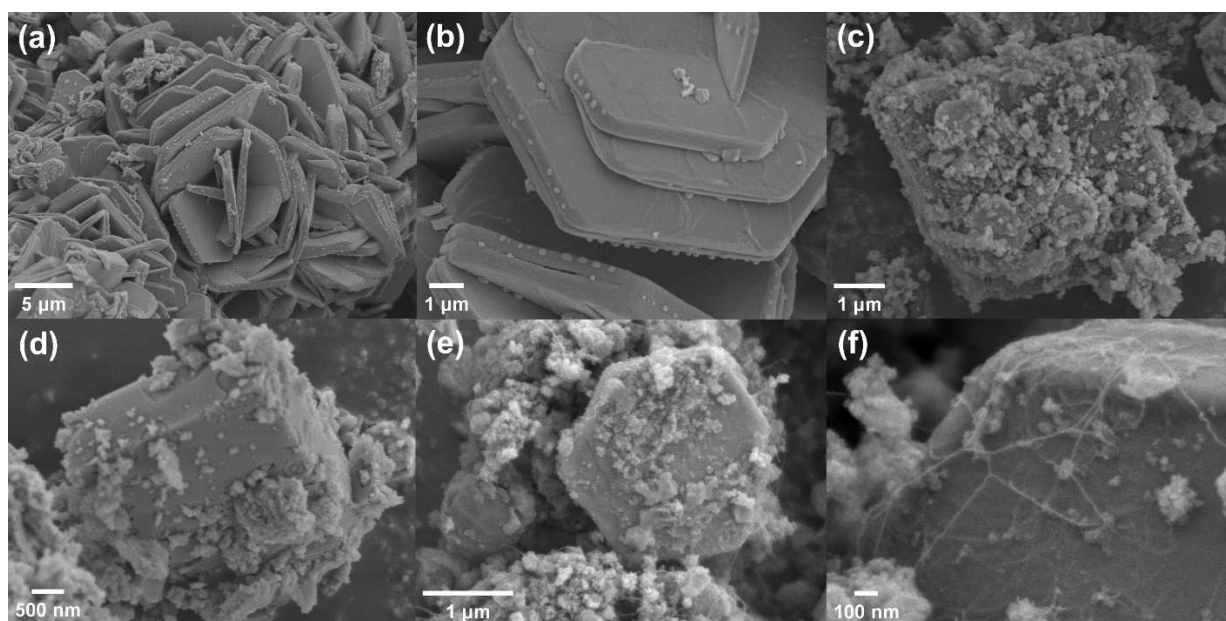


**Figure 2.** FESEM images of (a and b) $VSe_2$, (c and d) $VSe_2$/e-MXene and (e and f) $VSe_2$/e-MXene/CNT.
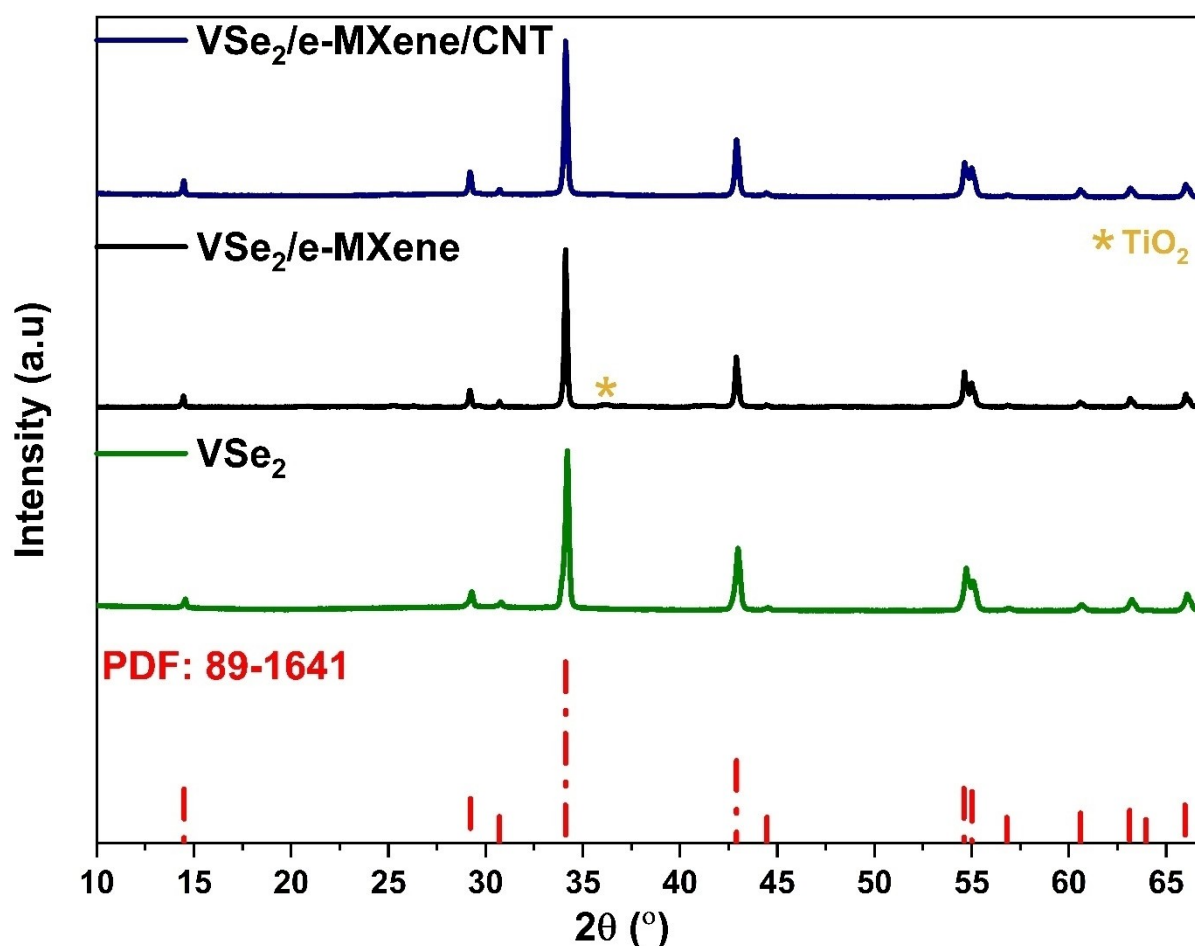
**Figure 3.** XRD pattern of $VSe_2$, $VSe_2$/e-MXene and $VSe_2$/e-MXene/CNT.

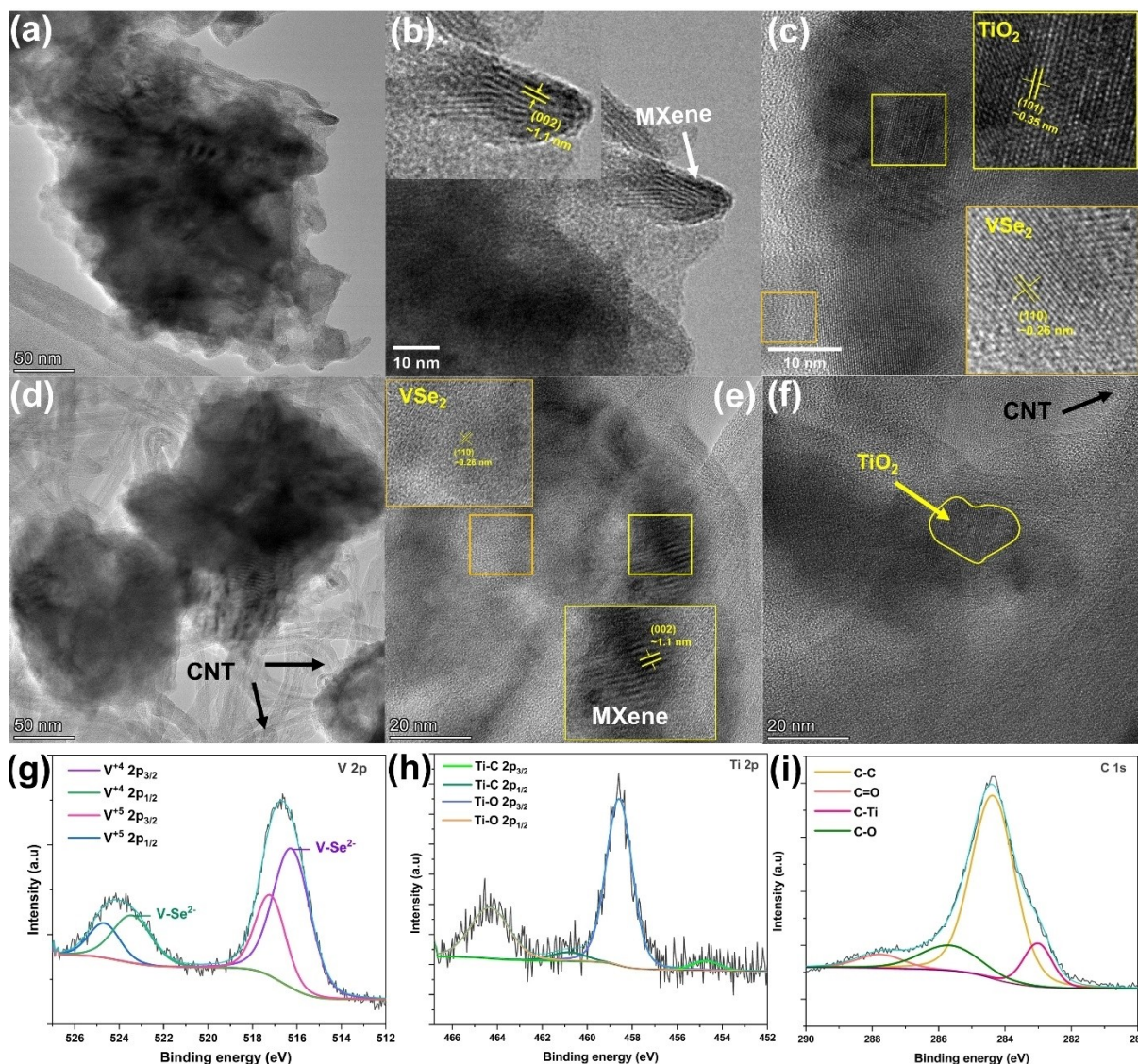trations. We observed low-intensity diffraction patterns of $TiO_2$ in $VSe_2$/e-MXene due to the obvious surface oxidation of MXene during the hydrothermal reaction. We made similar observations in our previous study while using multilayered $Ti_3C_2$ MXene, but the oxidation intensity is lower here. In the $VSe_2$/e-MXene/CNT ternary hybrid system, the $TiO_2$ peaks have disappeared. The presence of CNT may play a crucial role in limiting the undesired oxidation in the MXene structure during the synthesis.[35]

TEM analysis was used to extrapolate a clear picture of the microstructure in both binary and ternary hybrids. $VSe_2$/e-MXene shows a typical binary hybrid structure (Figure 4a). After the hydrothermal reaction, the interlayer distance of e-MXene is reduced to ~1.1 nm (Figure 4b) suggesting the absence of any $VSe_2$ nanoclusters growing separately between MXene layers.[36] It is also clear that the MXene structure is intact in the hybrid and there is not much restacking. HRTEM images confirm the presence of $VSe_2$ and $TiO_2$ (Figure 4c). The lattice fringes of each component in the sample were studied and identified the (110) plane of $VSe_2$ and (101) plane of $TiO_2$. The TEM images of $VSe_2$/e-MXene/CNT display a ternary hybrid composed of $VSe_2$, e-MXene and CNT (Figure 4d and e). In the HRTEM image, the interlayer distance of MXene remained unchanged compared to the hybrid structure confirming the structural integrity of

MXene in the ternary system. As we searched in other areas, the formation of $TiO_2$ nanoparticles can be found in the ternary hybrid also (Figure 4f). Here, the presence of $TiO_2$ is less frequent than in the binary system. This suggests that the construction of a ternary system limits the formation of $TiO_2$ nanoparticles on the MXene. Further studies are required to understand these observations.

XPS analysis is used to examine the chemical composition of the as-synthesised $VSe_2$/e-MXene/CNT. The survey spectrum of the $VSe_2$/MXene/CNT sample displayed in Figure S3a shows characteristic peaks of V, Se, Ti, C, and O. Two doublets have emerged in the deconvoluted V 2p spectra at 516.2/517.2 eV and 523.5/524.6 eV corresponding to V $2p_{3/2}$ and V $2p_{1/2}$ species, respectively (Figure 4g). The peaks at 516.2 and 523.5 eV can be attributed to the formation of the $V^{4+}$ state indicating a V–Se bonding.[37] Further, the deconvoluted Se 3d spectra show two distinct peaks at 54.6 and 55.5 eV representing $Se^{2-}3d_{5/2}$ and $Se^{2-}3d_{3/2}$ respectively (Figure S3b). Correlation with V 2p with deconvoluted Se 3d spectra confirms the formation of $VSe_2$ in the hybrid structure. In both V 2p and Se 3d the presence of their corresponding unavoidable oxide species is also noted.[37] In the Ti 2p spectra of $Ti_3C_2$ MXene, Ti–C species were observed at 454.7 and 460.8 eV confirming the structural integrity of MXene in the hybrid structure (Figure 4h).[38] Meanwhile, the

**Batteries & Supercaps**

Research Article
doi.org/10.1002/batt.202400466

**Chemistry Europe**
European Chemical
Societies Publishing

**Figure 4.** (a and b) TEM images and (c) HRTEM image of VSe$_2$/e-MXene. (d and e) TEM images and (f) HRTEM image of VSe$_2$/e-MXene/CNT. Deconvoluted XPS spectra of (g) V 2p, (h) Ti 2p and (i) C 1s of VSe$_2$/e-MXene/CNT.

peaks 458.5 and 464.3 eV correspond to the Ti–O species. Even though, the heterostructure formation has suppressed the degree of oxidation of the MXene, a certain level of undesired surface oxidation of MXene is yet to be controlled during the hydrothermal reaction. The peak at 530.1 eV of the O 1s spectra represents the Ti–O/V–O bonding, resonating with the oxidation of Ti and V noted earlier (Figure S3c). The peak at 531.6 eV originates from the C–Ti–O species due to the presence of the -O functional group on the MXene surface.[39] Besides that, O 1s spectra show two peaks at 530.9 and 532.2 eV representing C=O and C–O species. As for the C 1s spectra, peaks at 282.9, 284.3, 285.7, and 287.7 eV correspond to the C–Ti, C–C, C–O, and C=O bonds respectively (Figure 4i).

## 3.2. Electrochemical Analysis of VSe$_2$/e-MXene/CNT

The electrochemical analysis of all the samples was carried out in a conventional three-electrode setup with 0.5 M K$_2$SO$_4$ aqueous electrolyte. To analyse the effect of CNT we synthesised two ternary hybrids with varying CNT concentrations (see experimental section). The CV analysis revealed that the ternary hybrid has the largest enclosed area establishing its high electrochemical activity (Figure 5a). While comparing the two CNT ternary systems, sample with 30 mg showed better performance than the sample with 50 mg CNT. In high CNT concentrations, the agglomeration of CNT can limit the electrochemical performance. VSe$_2$ shows a quasi-rectangular CV profile pointing towards its pseudocapacitive contributions (Figure S4a). Similarly, VSe$_2$/e-MXene also shows a pseudocapacitive nature in its CV profile (Figure S4c). The ternary hybrid system showed more of a capacitive profile due to the obvious
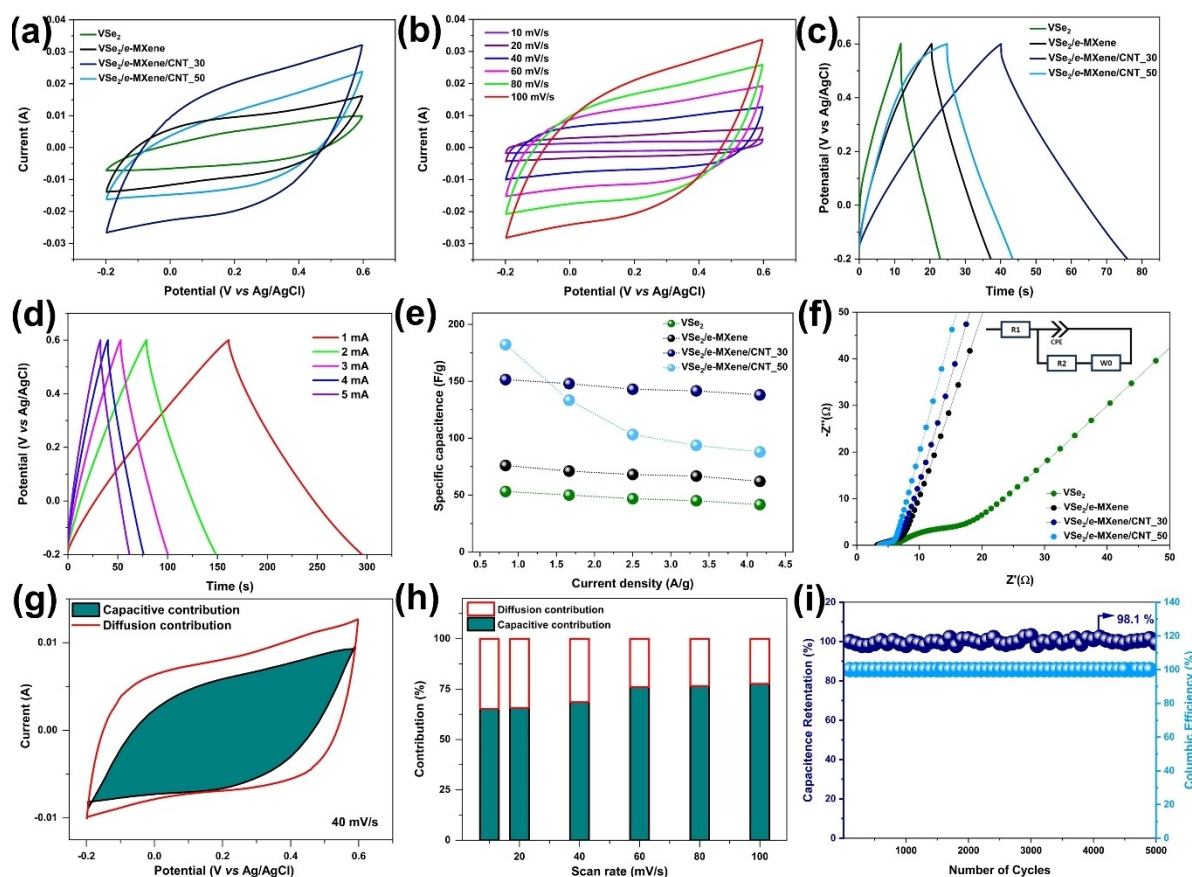
**Figure 5. Three-electrode analysis**. (a) comparative CV of all the electrodes at 100 mV/s, (b) CV profile of VSe$_2$/e-MXene/CNT_30 in various scan rates, (c) comparative GCD profile of all electrodes at 3 mA, (d) GCD profile of VSe$_2$/e-MXene/CNT_30 in various input currents, (e) specific capacitance vs current density plot, (f) Nyquist plot (inset: equivalent circuit), (g) deconvoluted CV using power law of VSe$_2$/e-MXene/CNT_30 at 40 mV/s, (h) capacitive and diffusive contributions in all scan rates and (i) cyclic stability of VSe$_2$/e-MXene/CNT_30.

EDL contributions from the CNT. Figure 5b depicts the VSe$_2$/e-MXene/CNT_30 CV curves in scan rates ranging from 10–100 mV/s. In all scan rates, the electrode retains its shape, highlighting its excellent reversibility. The GCD profile also follows a similar trend as the CV, underscoring the improved electrochemical activity of the VSe$_2$/e-MXene/CNT_30 electrode (Figure 5c). Figure 5d depicts the GCD profile of the VSe$_2$/e-MXene/CNT_30 electrode in applied current values increasing from 1–5 mA. The GCD profile does not show any potential independent region which emphasises the dominant capacitive behaviour of the electrode. In the GCD profile, the VSe$_2$/e-MXene/CNT_50 electrode exhibits a longer discharge time with a low coulombic efficiency of ~59% (Figure S4f). While evaluating the capacitance value, VSe$_2$/e-MXene/CNT_30 showed a maximum capacitance of 151 F/g at 1 mA, a 284% increase from pristine VSe$_2$ at a similar input current (Figure 5e). Moreover, the electrode showed a remarkable rate capability as it retained ~91% of its capacitance at the highest current density. Even though VSe$_2$/e-MXene/CNT_50 showed a higher capacitance (182 F/g), it suffers from low coulombic efficiency and underwhelming rate capability. EIS is used to extrapolate the kinetics of the electrochemical activity in the electrodes studied in this work. Nyquist plot of all electrodes is depicted in Figure 5f. Compared to pristine VSe$_2$ all the hybrid samples

showed capacitive behaviour. As CNT concentration increased the electrodes started to show a Nyquist profile similar to that of an ideal capacitor at the low frequency region as expected. After the incorporation of MXene, the R$_s$ value of the binary hybrid system is reduced emphasising the enhanced intrinsic conductivity of the electrode. With the addition of CNT, we observed no considerable change in the R$_s$ value. Similarly, the reduction in R$_{ct}$ values in the hybrid systems reveals their increased ion diffusion kinetics which correlates with the enhanced charge storage performance. VSe$_2$/e-MXene/CNT_30 has a smaller R$_{ct}$ than VSe$_2$/e-MXene and VSe$_2$, contributing to its improved interfacial activity. R$_s$ and R$_{ct}$ values of all the electrodes extracted from the Nyquist plot are summarised in Table S1.

To understand the charge storage mechanism, the CV profile of the VSe$_2$/e-MXene/CNT_30 electrode is deconvoluted using the power law into capacitive and diffusive contributions (Equations S3-S5). The deconvoluted CV establishes a capacitive dominant mechanism to the electrode (Figure 5g). Even at a low scan rate, the capacitive contribution of this particular electrode is ~65% and it increases to 77.6% at 100 mV/s (Figure 5h). The plausible cationic intercalation into the layers of pseudocapacitive VSe$_2$ and Ti$_3$C$_2$T$_x$ MXene emulates the diffusion contribution in the electrode. Due to relatively long

interaction time at the electrode-electrolyte interface during the low scan rates, the ion impregnation is more so is the diffusion contribution. The VSe$_2$/e-MXene/CNT_30 (now onwards we are simply representing it as VSe$_2$/e-MXene/CNT) electrode's cyclic stability was examined in 5000 GCD cycles at a specific current of 8 A/g (Figure 5i). The electrode maintained an excellent capacitance retention of 98.1 % after the cyclic study which is superior to pristine VSe$_2$ and VSe$_2$/MXene electrodes analysed in our previous study. The electrode also showed nearly 100 % coulombic efficiency during the cyclic study underscoring its remarkable reversibility.

The construction of a ternary hybrid structure provides a large amount of redox active sites and the presence of CNT multiplies the ionic activity. The emulated conductivity and shortened ionic channels are due to the synergised activity of each component in the ternary system. The multiple material interaction can reduce the surface oxidation of MXene to a degree but we are unable to establish the mechanism behind this and its contribution to the overall electrochemical performance of the electrode. We believe a simulated effect of all these factors are contributing towards the improved supercapacitor performance of the 3D ternary hybrid electrode material.

### 3.2.1. Performance of the Asymmetric Supercapacitor

An asymmetric supercapacitor (ASC) has been assembled to study the full cell performance of the VSe$_2$/ e-MXene/CNT electrode (Figure 6a). With a working window of $-0.2$–0.6 V (vs Ag/AgCl), VSe$_2$/e-MXene/CNT will be the positive electrode and MoS$_2$/MXene with a working window of $-1$ - $-0.2$ V (vs Ag/AgCl) will act as the negative electrode for the ASC assembly

(Figure 6b). MoS$_2$/MXene is a promising electrode material explored in our previous work.[40] The FESEM images of MoS$_2$/MXene show the MoS$_2$ nanosheets grown over accordion-type MXene to form a 3D hierarchical structure (Figure S5). Details of the full-cell ASC assembly are provided in the experimental section. The charge balance of both electrodes is achieved using Equation S6. The assembled device is tested in various working windows and 1.6 V is optimised as the stable working window of the ASC (Figure S6a). The VSe$_2$/MXene/CNT//MoS$_2$/MXene ASC showed a consistent CV profile during all scan rates exhibiting the reversibility and capacitive behaviour of the cell (Figure 6c). The GCD profile of the ASC in specific currents ranging from 1.6–8 A/g is provided in Figure 6d. The GCD curves showed a quasi-triangular shape without any potential independent plateaus underscoring the dominant capacitive behaviour of the ASC. The ASC's capacitance, energy, and power density were calculated using Equation S1–S2 from the GCD profile. The ASC showed a maximum capacitance of 101 F/g at a specific current of 1.6 A/g (Figure S6b). Ragone plot, one of the key features of any ASC is provided in Figure 6e. The VSe$_2$/MXene/CNT//MoS$_2$/MXene ASC exhibited a maximum energy density of 35.91 Wh/kg at a power density of 1280 W/kg which is on par with recent studies (Table 1). Further, the ASC retained an energy density of 24.17 Wh/kg at a maximum power density of 6350 W/kg showing the excellent rate capability of the device. The ASC showed an outstanding ~99 % capacitance retention after 5000 GCD cycles with nearly 100 % coulombic efficiency (Figure 6f).
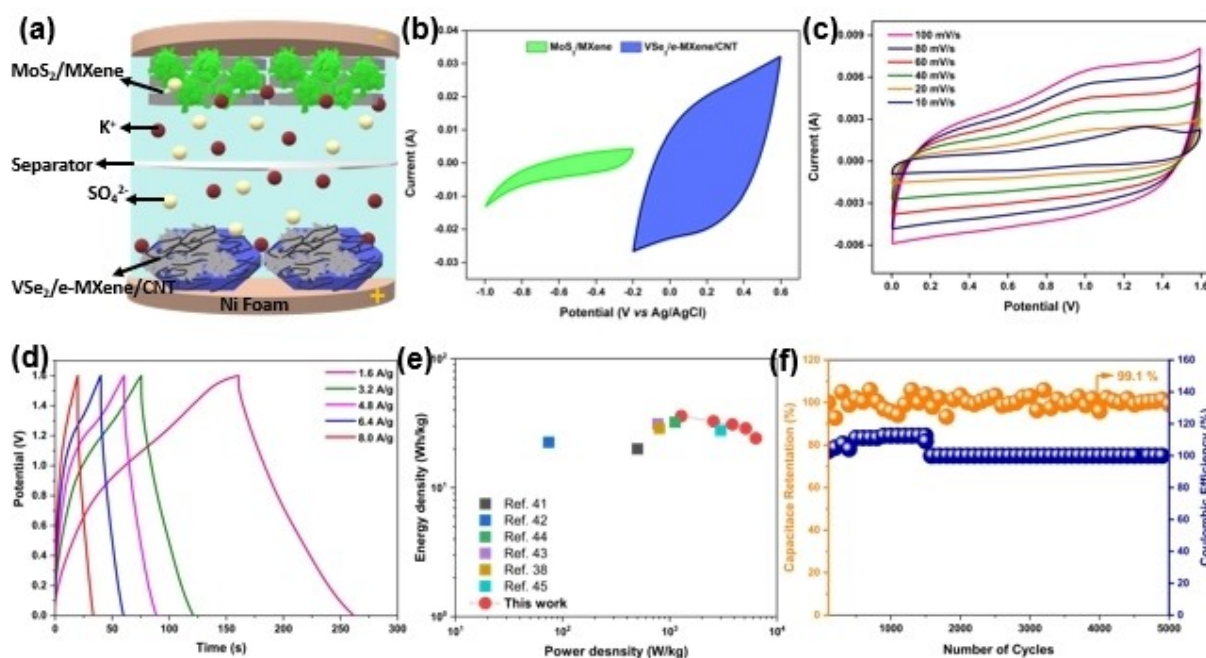


**Figure 6. Performance of the ASC.** (a) Illustration of the ASC construction, (b) CVs of both the positive electrode and the negative electrode at 100 mV/s, (c) CV profile of the ASC in varying scan rates, (d) GCD profile of the ASC in varying current densities, (e) Ragone plot and (f) cyclic performance of the ASC.

**Batteries & Supercaps**

Research Article
doi.org/10.1002/batt.202400466

Chemistry
Europe
European Chemical
Societies Publishing

**Table 1.** Comparative energy storage performance of VSe$_2$/e-MXene/CNTs//MoS$_2$/MXene with other reported asymmetric supercapacitors.

| Electrode (ASC) | Electrolyte | Operating window (V) | energy density (W h/kg) at power density (W/kg) | Cycle stability | Ref. |
|---|---|---|---|---|---|
| Ni–S/1d-Ti$_3$C$_2$//d-Ti$_3$ | 6 M KOH | 1.9 | 20 at 500 | 66.5% after 5000 cycles | [41] |
| Co$_3$O$_4$@NF//MX-5@PCNF | 2 M KOH | 1.5 | 22.53 at 74.2 | 96.4% after 10,000 cycles | [42] |
| NiCo$_2$S$_4$@VS$_2$//AC | 3 M KOH | 1.55 | 31.2 at 775 | - | [43] |
| MoS$_2$/MWCNT//VSe$_2$/MWCNT | 0.5 M K$_2$SO$_4$ | 1.4 | 32.18 at 1121 | 98% after 5000 cycles | [44] |
| MXene/CoS$_2$(CCH)//rGO | 2 M KOH | 1.6 | 28.8 at 800 | 98% after 5000 cycles | [38] |
| VS$_2$//C–Fe/PANI | 6 M KOH | 1.7 | 27.8 at 2991.5 | 95% (10000 cycles) | [45] |
| VSe$_2$-MXene-SWCNTs//MoS$_2$-MXene | 0.5 M K$_2$SO$_4$ | 1.6 | 35.91 at 1280 | 99.1% after 5000 cycles | This work |

## 4. Conclusions

In summary, a 3D VSe$_2$/e-MXene/CNT ternary hybrid structure is successfully synthesised by a one-pot hydrothermal reaction. The material characterisation revealed that the ternary hybrid system can reduce the unwanted oxidation of the MXene surface to a degree during the hydrothermal reaction. In the three-electrode evaluation, the VSe$_2$/e-MXene/CNT electrode showed enhanced electrochemical performance owing to the synergistic interplayed effect triggered by VSe$_2$, Ti$_3$C$_2$T$_x$ MXene and SWCNT network. The 3D network in the ternary hybrid improved electronic conductivity, shortening the ionic pathways and providing more active electrolyte sites. Further, the VSe$_2$/MXene/CNT electrode was incorporated as the positive electrode in an ASC to evaluate its performance in a full-cell configuration. The aqueous electrolyte-based ASC showed a stable working window of 1.6 V without any electrolyte degradation. The device exhibited an attractive energy density of 35.91 Wh/kg at a power density of 1280 W/kg with a remarkable cyclic performance. This work encapsulates bright application prospects of MXenes and TMDs combination for supercapacitors. This work was conceived and formulated as an effort from our side to accelerate the research in TMDs and MXene-based energy storage devices. Further, it also paves cobblestones for the development of modern pseudocapacitors-based asymmetric supercapacitors and aqueous supercapacitors.

## Conflict of Interests

Authors declare no conflict of interest.

## Data Availability Statement

The data that support the findings of this study are available from the corresponding author upon reasonable request.

[1] K. Naoi, W. Naoi, S. Aoyagi, J. Miyamoto, T. Kamino, *Acc. Chem. Res.* **2013**, *46*(5), 1075–1083.
[2] W. Raza, F. Ali, N. Raza, Y. Luo, K.-H. Kim, J. Yang, S. Kumar, A. Mehmood, E. E. Kwon, *Nano Energy* **2018**, *52*, 441–473.
[3] M. Salanne, B. Rotenberg, K. Naoi, K. Kaneko, P.-L. Taberna, C. P. Grey, B. Dunn, P. Simon, *Nat. Energy* **2016**, *1*(6), 16070.
[4] M. Ali, A. M. Afzal, M. W. Iqbal, S. Mumtaz, M. Imran, F. Ashraf, A. Ur Rehman, F. Muhammad, *Intl. J. Energy Res.* **2022**, *46*(15), 22336–22364.
[5] N. Joseph, P. M. Shafi, A. C. Bose, *Energy Fuels* **2020**, *34*(6), 6558–6597.
[6] X. Zhang, H. Zhang, C. Li, K. Wang, X. Sun, Y. Ma, *RSC Adv.* **2014**, *4*(86), 45862–45884.
[7] M. G. Hahm, A. Leela Mohana Reddy, D. P. Cole, M. Rivera, J. A. Vento, J. Nam, H. Y. Jung, Y. L. Kim, N. T. Narayanan, D. P. Hashim, C. Galande, Y. J. Jung, M. Bundy, S. Karna, P. M. Ajayan, R. Vajtai, *Nano Lett.* **2012**, *12*(11), 5616–5621.
[8] M. Cossutta, V. Vretenar, T. A. Centeno, P. Kotrusz, J. McKechnie, S. J. Pickering, *J. Cleaner Prod.* **2020**, *242*, 118468.
[9] J. Wei, M. Sajjad, J. Zhang, D. Li, Z. Mao, *Surf. Interfaces* **2023**, *42*, 103334.
[10] W. A. Haider, M. Tahir, L. He, H. A. Mirza, R. Zhu, Y. Han, L. Mai, *ACS Cent. Sci.* **2020**, *6*(11), 1901–1915.
[11] K. R. G. Lim, M. Shekhirev, B. C. Wyatt, B. Anasori, Y. Gogotsi, Z. W. Seh, *Nat. Synth.* **2022**, *1*(8), 601–614.
[12] C. E. Shuck, A. Sarycheva, M. Anayee, A. Levitt, Y. Zhu, S. Uzun, V. Balitskiy, V. Zahorodna, O. Gogotsi, Y. Gogotsi, *Adv. Eng. Mater.* **2020**, *22*(3), 1901241.
[13] A. S. Levitt, M. Alhabeb, C. B. Hatter, A. Sarycheva, G. Dion, Y. Gogotsi, *J. Mater. Chem. A* **2019**, *7*(1), 269–277.

[14] N. K., P. S., S. M. Jeong, C. S. Rout, *Energy Adv.* **2024**. 10.1039.D3YA00502J.

[15] Z. Fan, Y. Wang, Z. Xie, D. Wang, Y. Yuan, H. Kang, B. Su, Z. Cheng, Y. Liu, *Adv. Sci. (Weinh)* **2018**, *5*(10), 1800750.

[16] L. Shen, X. Zhou, X. Zhang, Y. Zhang, Y. Liu, W. Wang, W. Si, X. Dong, *J. Mater. Chem. A* **2018**, *6*(46), 23513–23520.

[17] X. Xie, M.-Q. Zhao, B. Anasori, K. Maleski, C. E. Ren, J. Li, B. W. Byles, E. Pomerantseva, G. Wang, Y. Gogotsi, *Nano Energy* **2016**, *26*, 513–523.

[18] A. Sharma, P. Mane, B. Chakraborty, C. S. Rout, *ACS Appl. Energy Mater.* **2021**, *4*(12), 14198–14209.

[19] S. Raj Ka, P. Mane, S. Radhakrishnan, B. Chakraborty, C. S. Rout, *ACS Appl. Nano Mater.* **2022**, *5*(3), 4423–4436.

[20] W. Hou, Y. Sun, Y. Zhang, T. Wang, L. Wu, Y. Du, W. Zhong, *J. Alloys Compd.* **2021**, *859*, 157797.

[21] S. Tanwar, A. Arya, A. Gaur, A. L. Sharma, *J. Phys.: Condens. Matter* **2021**, *33*(30), 303002.

[22] X. Wu, Z.-B. Zhai, K.-J. Huang, R.-R. Ren, F. Wang, *J. Power Sources* **2020**, *448*, 227399.

[23] H. Zhang, D. Xiong, C. Xu, C. Yie, L. Zeng, Z. Feng, M. He, Q. Liu, *Electrochim. Acta* **2022**, *421*, 140487.

[24] H. Li, J. Li, L. Ma, X. Zhang, J. Li, J. Li, T. Lu, L. Pan, *J. Mater. Chem. A* **2023**, *11*(6), 2836–2847.

[25] W. Wang, X. Wang, L. Chen, D. Lu, W. Zhou, Y. Li, *Chem. Eng. J.* **2023**, *461*, 142100.

[26] C. Wang, X. Wu, H. Xu, Y. Zhu, F. Liang, C. Luo, Y. Xia, X. Xie, J. Zhang, C. Duan, *Appl Phys Lett* **2019**, *114*(2), 023902.

[27] K. A. Sree Raj, A. S. Shajahan, B. Chakraborty, C. S. Rout, *Chem. A Eur. J.* **2020**, *26*(29), 6662–6669.

[28] M. Narayanasamy, L. Hu, B. Kirubasankar, Z. Liu, S. Angaiah, C. Yan, *J. Alloys Compd.* **2021**, *882*, 160704.

[29] K. A. Sree Raj, A. S. Shajahan, B. Chakraborty, C. S. Rout, *Chem. A Eur. J.* **2020**, *26*(29), 6662–6669.

[30] Q. Zhu, M. Shao, S. H. Yu, X. Wang, Z. Tang, B. Chen, H. Cheng, Z. Lu, D. Chua, H. Pan, *ACS Appl. Energy Mater.* **2019**, *2*(1), 644–653.

[31] S. R. Marri, S. Ratha, C. S. Rout, J. N. Behera, *Chem. Commun.* **2017**, *53*(1), 228–231.

[32] K. A., S. R., K. Pramoda, C. S. Rout, *J. Mater. Chem. C* **2023**, *1(7)*, 2565–2573.

[33] K. A., S. R., A. S. Shajahan, B. Chakraborty, C. S. Rout, *RSC Adv.* **2020**, *10(53)*, 31712–31719.

[34] C. Hao, Y. Liao, Y. Wu, Y. An, J. Lin, Z. Gu, M. Jiang, S. Hu, X. Wang, *J. Phys. Chem. Solids* **2020**, *136*, 109141.

[35] S. Wei, Y. Fu, M. Liu, H. Yue, S. Park, Y. H. Lee, H. Li, F. Yao, *npj 2D Mater. Appl.* **2022**, *6*(1), 25.

[36] X. Wang, H. Li, H. Li, S. Lin, W. Ding, X. Zhu, Z. Sheng, H. Wang, X. Zhu, Y. Sun, *Adv. Funct. Mater.* **2020**, *30*(15), 0190302.

[37] L. Wang, Z. Wu, M. Jiang, J. Lu, Q. Huang, Y. Zhang, L. Fu, M. Wu, Y. Wu, *J. Mater. Chem. A* **2020**, *8*(18), 9313–9321.

[38] H. Liu, R. Hu, J. Qi, Y. Sui, Y. He, Q. Meng, F. Wei, Y. Ren, Y. Zhao, W. Wei, *Adv. Mater. Inter.* **2020**, *7*(6), 1901659.

[39] S. Wei, Y. Fu, M. Liu, H. Yue, S. Park, Y. H. Lee, H. Li, F. Yao, *npj 2D Mater. Appl.* **2022**, *6*(1), 25.

[40] K. A., S. R., N. Barman, S. Radhakrishnan, R. Thapa, C. S. Rout, *J. Mater. Chem. A* **2022**, *10*(44), 23590–23602.

[41] Y. Luo, C. Yang, Y. Tian, Y. Tang, X. Yin, W. Que, *J. Power Sources* **2020**, *450*, 227694.

[42] S, C., S. Upadhyay, N. C. Joshi, N. Kumar, P. Choudhary, N. Sharma, V. N. Thakur, *FlatChem* **2023**, *37*, 100456.

[43] Z. Zhang, X. Huang, H. Wang, S. H. Teo, T. Ma, *J. Alloys Compd.* **2019**, *771*, 274–280.

[44] J. Li, X. Yuan, C. Lin, Y. Yang, L. Xu, X. Du, J. Xie, J. Lin, J. Sun, *Adv. Energy Mater.* **2017**, *7*(15), 1602725.

[45] M. N. Rantho, M. J. Madito, F. O. Ochai-Ejeh, N. Manyala, *Electrochim. Acta* **2018**, *260*, 11–23.